International Journal of Heat and Mass Transfer 197 (2022) 123326

Contents lists available at ScienceDirect

International Journal of Heat and Mass Transfer

journal homepage: www.elsevier.com/locate/hmt

A computational model for interfacial heat and mass transfer in two-phase flows using a phase field method

Shahab Mirjalili*, Suhas S. Jain, Ali Mani

Center for Turbulence Research, Stanford University, Stanford, CA 94305, USA

ARTICLE INFO

Article history:
Received 2 June 2022
Revised 27 July 2022
Accepted 3 August 2022

Keywords:
Two-phase flows
Phase field
Heat transfer
Mass transfer
Diffuse interface

ABSTRACT

Two-phase flows involving heat/mass transfer are widespread in industrial and environmental applications such as chemical reactors, bubbly flows, combustion, boiling, carbon sequestration, and ocean-atmosphere exchanges. It is therefore important to accurately predict the rate of heat/mass transfer across capillary interfaces via numerical simulations. Due to the absence of a well-defined interface, modeling interfacial transfer between two phases is particularly challenging for phase field (diffuse interface) models. In the context of second-order conservative phase field models, by assuming a microstructure that is consistent with the interfacial profile, we use perturbation theory and asymptotic analysis to derive interfacial heat/mass exchange terms that are consistent extensions of the underlying phase field equations. The developed two-scalar model is conservative, preserves positivity of total scalar concentration, and correctly predicts the transient and equilibrium solutions in all limits of diffusivity ratio. Additionally, we demonstrate that by assuming thermodynamic equilibrium in the microstructure, a more reduced model in the form of a one-scalar equation is derived. Several canonical and realistic simulations are presented to assess the consistency, accuracy, and convergence of the models. Crucially, while the one-scalar and two-scalar models both perform well when the two phases have comparable diffusivities, the two-scalar model is found to be much more accurate for realistic problems with large diffusivity ratios as it prevents unphysical leakage of heat/mass.

1. Introduction

Two-phase flow problems involving interfacial transfer of heat and mass are ubiquitous. Accurate prediction of interfacial heat transfer is critical in many industrial settings, including direct-contact heat exchangers [1], distillation processes [2], combustion [3], atomization of sprays [4] and all problems that involve evaporation and boiling. Industrial applications where interfacial mass transfer plays an important role include bubble column reactors [5], oxygenation of aqueous systems [6], metal refining, gas scrubbing and waste water treatments in bioreactors [7]. Interfacial mass and heat transfer is also of significant interest in many natural phenomena, including rain formation and atmosphere-ocean heat/mass exchange [e.g., oceanic carbon sequestration [8]].

To numerically predict the evolution of heat and mass in the above applications, it is critical to accurately compute (1) the evolution of the interface between two phases, (2) the transport—i.e., diffusion and advection—of heat/mass within the bulk of each phase, and (3) their transfer across the interface. There are plenty of effective and accurate numerical methods for capturing the interfaces in two-phase flows [9]. While sharp interface methods such as level-set (LS) and volume-of-fluid (VOF) methods have traditionally received the most attention, diffuse interface methods, also known as phase field methods, have recently become popular for simulating two-phase flows. This rise in popularity is due to their simplicity in implementation, parallel scalability and the possibility of using more standard spatial discretization schemes because of the diffuse interfaces that result in smooth fields [9,10]. There has been a fair amount of previous work on computational models for transport and interfacial transfer of heat/mass in two-phase systems. These developments have been mostly for sharp interface methods. As we will show, there is an equivalence between the problems of heat transfer and mass transfer, and a numerical model designed for one can be reformulated for the other.

Broadly, the proposed models in the literature for either heat transfer problems or mass transfer problems can be classified into one-scalar models and two-scalar models. The former is based on the assumption of thermal equilibrium for heat and chemical equilibrium for mass at the interface—continuity of temperature for heat and Henry's law for mass. Examples of one-scalar models

* Corresponding author.
E-mail addresses: ssmirjal@stanford.edu (S. Mirjalili), sjsuresh@stanford.edu (S.S. Jain), alimani@stanford.edu (A. Mani).

https://doi.org/10.1016/j.ijheatmasstransfer.2022.123326
0017-9310/

Nomenclature

Latin letters

$\bar{\tilde{c}}_i$	mean local scalar concentration in phase i
$\tilde{c}_i'$	local concentration perturbation in phase i
K_{eq}	concentration ratio across interface at equilibrium
c_i	amount of scalar in phase i per total volume
h	thickness of each layer in microstructure
Sc	Schmidt number
$\tilde{c}_i$	local scalar concentration in phase i
D_i	diffusivity of scalar in phase i
A	free parameter representing an inverse time scale to thermodynamic equilibrium
D_m	mixed diffusivity
k_i	heat conductivity in phase i
$C_{p,i}$	specific heat capacity of phase i
H	Henry coefficient
J	inter-phase transfer terms
g	gravitational constant
t	time
$\vec{u}$	velocity
$\vec{n}$	normal vector
$\tilde{q}_i$	local heat content in phase i

Greek letters

ρ_i	density of phase i
μ_i	viscosity of phase i
ν	kinematic viscosity
ϕ	phase field variable
ϵ	free parameter in phase field equation controlling interface thickness
γ	free parameter in phase field equation controlling strength of right hand side terms

Acronyms

VOF	Volume of fluid
LS	Level set
CDI	Conservative diffuse interface
CPF	Conservative phase field
RHS	right hand side
PDE	partial differential equation
LHS	left hand side
LS	Level set

Subscripts

eff	effective
max	maximum
os	one-scalar

can be found in [11–13] for VOF methods; [14–16] for LS methods; and [17] for phase field methods. In these methods, a single equation is solved to compute the evolution of heat/mass within the two phases. The main drawback of one-scalar models is unphysical leakage of heat/mass in situations where the resistance (diffusivity) ratio between the two phases is large. Such situations are common in many practical gas-liquid two-phase flows. This has motivated researchers to develop two-scalar models that can prevent leakage and yield more accurate transient solutions, as they do not enforce thermodynamic equilibrium at the interface but rather ensure that the steady solution to the model achieves thermodynamic equilibrium. Such models solve one equation for the heat/mass stored within each phase, resulting in two-scalar equations for two-phase flows. Notable examples of such models can be found in [18–22]; all of these models are designed for VOF interface capturing schemes and most of them can also be adapted to other sharp interface schemes, i.e., LS methods.

The diffusivity ratio between the two phases is very large in many two-phase systems for heat and/or mass transport. As a result, in such systems the heat/mass is effectively confined to one of the phases. Some researchers have therefore developed transport models that do not account for interfacial transfer [23,24]. In particular, [24] derived one such model for second-order phase field methods that prevents leakage across the interfaces, preserves the positivity of the scalar (heat/mass), and achieves an equilibrium profile for the scalar that is consistent with the phase field solution profile. In this work, we extend the work of [24] by analytically deriving the interfacial transfer terms to obtain models that account for conjugate transfer of heat/mass. In particular, by assuming a geometrical microstructure for the interface, we use perturbation analysis to obtain transfer terms for the two-scalar model that are consistent with the phase field model. The derived two-scalar model can be applied to problems with arbitrary diffusivity ratios between the two phases. Specifically, in the limit of zero diffusivity ratios, the derived model reduces to that of [24]. Additionally, by assuming thermodynamic equilibrium at the interface, we also derive a consistent one-scalar model that performs well when the two phases have comparable diffusivity for heat/mass but suffers from unphysical leakage when the diffusivity ratio is large.

In Section 2, we present the governing equations, explaining how the problems of heat and mass transport in two-phase flows are equivalent, even discretely. The model requirements are enlisted in Section 3, and the microstructure is introduced in Section 4. Using this microscopic model for the diffuse interface, we derive the models for interfacial transfer of heat/mass in Section 5. After describing the computational approach and the positivity properties of the models, we present several numerical tests of the models for validation in Section 6. Finally, we summarize our findings in Section 7.

2. Governing equations

Capillary interfaces are $O(1\text{nm})$ in subcritical conditions and are thus assumed sharp on continuum scale. The governing equations for the evolution of heat/mass in a two-phase system consist of transport equations that hold within the bulk of each phase, in addition to boundary conditions at the interface, connecting the bulks lying on either side. The transport equation for dilute chemical species in the bulk fluids is an advection-diffusion equation. For mass transport, within the bulk of phase i we have

$$\frac{\partial \tilde{c}_i}{\partial t} + \nabla \cdot (\vec{u}\tilde{c}_i) = \nabla \cdot (D_i \nabla \tilde{c}_i), \tag{1}$$

where $i = 1, 2$ represents the phase index, the diffusivity in each phase is denoted by D_i, and $\tilde{c}_i$ is the local species concentration in phase i defined as amount of the species per unit volume of phase i. At the interface, mass balance implies continuity of the fluxes normal to the interface,

$$D_1 \nabla_n \tilde{c}_1 = D_2 \nabla_n \tilde{c}_2. \tag{2}$$

The second-order partial differential equation (PDE) given in Eq. (1) requires one more boundary condition, which comes from chemical equilibrium at the interface, modeled by Henry's law,

$$\frac{\tilde{c}_1}{\tilde{c}_2} = H, \tag{3}$$

where H is the Henry coefficient, assumed to be a constant.

The equations for heat transport can be formulated in an equivalent way if we write them in terms of local heat content, $\tilde{q} = \rho C_p T$, where ρ, C_p, and T are the density, specific heat capacity, and temperature, respectively. With this, heat transport in the bulk of phase i is given by

$$\frac{\partial \tilde{q}_i}{\partial t} + \nabla \cdot (\vec{u}\tilde{q}_i) = \nabla \cdot \left(\frac{k_i}{\rho_i C_{p,i}} \nabla \tilde{q}_i \right), \tag{4}$$

where k is the heat conductivity. Heat balance at the interface gives

$$\frac{k_1}{\rho_1 C_{p,1}} \nabla_n \tilde{q}_1 = \frac{k_2}{\rho_2 C_{p,2}} \nabla_n \tilde{q}_2, \tag{5}$$

and thermal equilibrium can be written as

$$\frac{\tilde{q}_1}{\tilde{q}_2} = \frac{\rho_1 C_{p,1}}{\rho_2 C_{p,2}}. \tag{6}$$

The one-to-one correspondence between Eqs. (1)–(3) for mass and Eqs. (4)–(6) for heat is clear. As such, we utilize these forms of the equations to derive a generalized model that can apply to both mass and heat, and we use the term scalar to refer to both species concentration and heat content. It is worth remarking that the aforementioned formulation is based on the conserved variable. An equally valid approach would be to solve for the variable that is continuous across the interface, i.e., chemical potential for mass and temperature for heat. However, this approach is not preferred since it loses the discrete conservation property inherent in the former approach. For more details on the governing equations in continuum modeling of mass transfer of a dilute species and heat transfer in a two-phase system refer to [11,25,26].

In this work, we neglect change in volume due to mass transfer. This is justified when the solute is in the dilute limit. Additionally, while the models we develop herein allow for simulation of problems in which heat and mass transfer mechanisms are coupled—e.g., Henry's constant or mass diffusivity depending on temperature—studying such problems is beyond the scope of the present work. Finally, phase change is not considered; thus, the scalar evolution equation for heat or mass is one-way coupled to the phase field and momentum transport equations. We concern ourselves with incompressible two-phase flows and second-order phase field models that result in hyperbolic tangent interfacial profiles at equilibrium. These models include phase field models that are based on the Allen-Cahn equations [27], such as [28,29], the conservative phase field (CDI/CPF) model developed by [30,31], and the accurate conservative phase field model by [32]. In this work, the CDI model by [30,31] is used, which can be written as

$$\frac{\partial \phi}{\partial t} + \nabla \cdot (\vec{u}\phi) = \nabla \cdot \left[\gamma \left(\epsilon \nabla \phi - \phi(1-\phi) \frac{\nabla \phi}{|\nabla \phi|} \right) \right]. \tag{7}$$

In Eq. (7), ϵ is the parameter that controls the diffuse interface thickness while γ is the other free parameter of the model which determines the strength of the right hand side terms, and ϕ is the phase field variable which is a smoothly varying function that can be interpreted as volume fraction of phase 1—fluid of pure phase 1 has $\phi = 1$, while fluid of pure phase 2 has $\phi = 0$. The main advantage of this equation is that it allows accurate and robust prediction of the interface position during advection, while maintaining its interfacial thickness because of the presence of the non-linear sharpening term [33]. Moreover, compared to phase field models based on the Cahn-Hilliard equation, which are also in conservative form, CDI models based on Eq. (7) boast noteworthy advantages [33]. First, because of its boundedness property and conservation, CDI does not suffer from the artificial shrinkage of drops/bubble observed in solutions to the Cahn-Hiliard equation [34]. Second, as opposed to the Cahn-Hilliard equation, CDI does not result in artificial coarsening of drops/bubbles. Lastly, solving a second-order PDE is numerically convenient compared to solving the fourth order PDE in Cahn-Hilliard models. Note that the models derived in this work can also be applied to second-order diffuse interface methods in compressible flows which attain hyperbolic tangent equilibrium profiles (see for instance [35] and references therein). This is because the transport of scalars is independent of whether the flow is compressible or incompressible.

3. Model requirements

Eqs. 1 –6 can be readily applied to sharp interface methods. However, the concepts of bulk fluids and interfaces are not as well defined in phase field methods. Since in phase field models any point in space and time is a mixture of two immiscible phases, the governing equations introduced above do not directly apply. Rather, a model must be derived. In this work, we seek a model that satisfies the following requirements:

- Conservation: scalar must be locally and globally conserved in a continuous and discrete sense.
- Generalizability: the model must apply to all second-order phase field methods with hyperbolic tangent equilibrium profiles and be usable for both heat and mass transfer.
- Consistency: the model should
  1. Reduce to the model presented in [24] when scalar diffusivity is zero in one of the phases.
  2. Asymptote to bulk equations given in Eqs. (1) and (4) away from the interfaces (ϕ tending to 0 or 1).
  3. Be equivalent to a single phase flow when the two phases have equal diffusivities (and other relevant material properties).
  4. Predict long-time equilibrium profiles correctly (e.g., linear/flat in 1D)
  5. Prevent unphysical leakage in the practical limit of large diffusivity ratios (e.g., $\mathcal{O}(10^4)$ for carbon dioxide transport in a water-air system).
- Convergence: as the mesh is refined and the interfacial region is made thinner, the model should converge to the true sharp interface solution.
- Positivity: physical constraints such as positivity of chemical species concentration must hold discretely.

To obtain a set of equations that result in a consistent and robust model for phase field methods, we assume an interfacial microstructure compatible with a diffuse interface and apply the above equations to control volumes containing sharp interfaces in the microstructure to derive the upscaled equations.

4. Microscopic model

In diffuse interface methods, a sharp interface is artificially thickened to the order of the grid size for numerical purposes. However, Eqs. (1)-(6) cannot be directly applied to diffuse interfaces as they require presence of sharply defined phase boundaries. In order to eliminate the ambiguity in the governing equations for a diffuse interface between two immiscible phases, one can assume that the diffuse interface region has a microstructure consisting of well-defined sharp interfaces. In particular, in this work, in order to guide our intuition in the model derivation process, we offer a geometrical microstructure that would allow quantitative interpretation of a diffuse interface. This geometric microstructure makes the model derivation amenable to pen and paper analysis. Consideration of sharp interfaces for the microstructure can also be justified given that all diffuse interface models define the phase field variable to represent the volume fraction, as opposed to mass fraction. This definition suggests that for any differential element of the domain a portion of the volume is occupied by fluid 1 and a portion is occupied by fluid 2. This mindset, inevitably requires an assumed microstructure with sharp interfaces, whose homogenized representation is capture by the diffuse interface model. It should be remarked that analogous to the diffuse interface equations, this microstructure is not physical. Moreover, existence of a microstructure is not necessary for derivation of interfacial transfer models. Nevertheless, we take advantage of the assumed microstructure as an intermediate step in our derivation

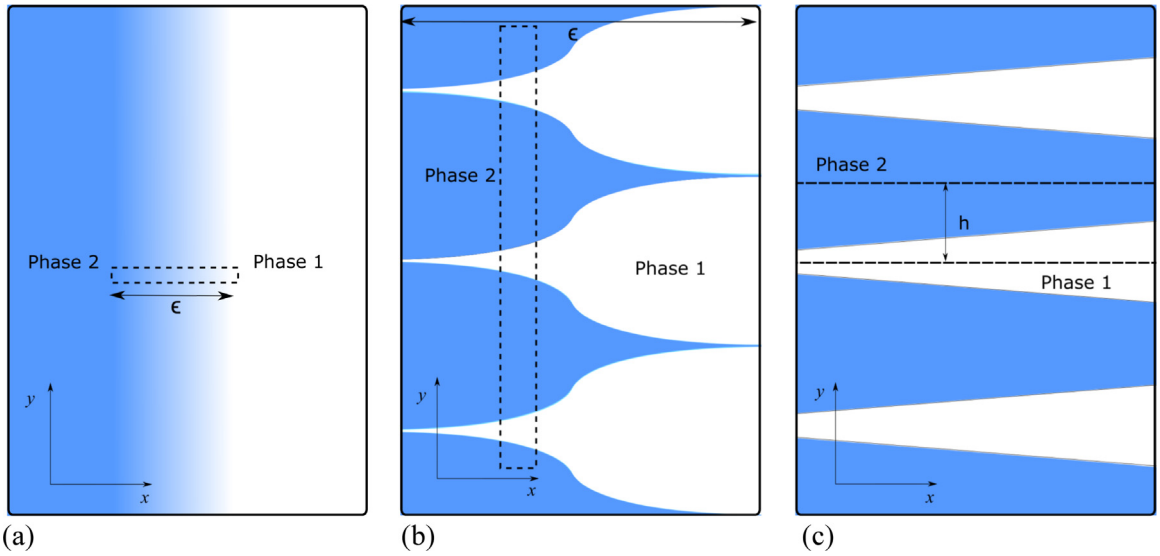

Fig. 1. Schematic depiction of (a) a 1D diffuse interface, (b) the microstructure when one zooms in on a narrow window on the diffuse interface and (c) a close-up view of the microstructure, schematically showing that the fingers are assumed to be thin structures.

to enforce the conditions enlisted in Section 3. The assumed microstucture is shown schematically in Fig. 1. This figure displays a one-dimensional diffuse interface with various levels of zoom-in. Fig. 1(a) shows the smooth transition from one phase to the other. By zooming in onto the thin box with width $\mathcal{O}(\epsilon)$ within the transition zone of this figure, we can see the assumed microstructure. This microstructure, shown schematically in Fig. 1(b), consists of fingers of one pure phase extending into the other. It is worth emphasizing that the interfaces shown in Fig. 1(b) are sharp interfaces that separate pure phases from one another. As such, Eqs. 1–6 can be applied at this level. In accordance with the phase field models of interest, the fingers are assumed to have hyperbolic tangent profiles, consistent with the equilibrium solution to Eq. (7). We also intentionally assume that the thickness of the fingers is very small compared to the thickness of the diffuse interface (transition zone). In other words, Fig. 1(b) is highly stretched in the y direction. Zooming in on the box shown in Fig. 1(b), a more accurate picture of the local microstructure can be obtained, shown schematically in Fig. 1(c). This figure demonstrates that the microstructure consists of long and thin structures with thickness h, where $h \ll \epsilon$. We point that the microstructure matching the phase field function is not unique. It might be possible to assume other structures, e.g., involving bubbles of one fluid into the other fluid, with bubble size and numbers diminishing as one moves away from the interface. However, we identified the proposed microstructure most suitable for analytical derivations.

5. Model derivation

Two-scalar models are necessary for capturing species concentration or heat content when the interface is not at thermodynamic equilibrium and/or the diffusivity (resistance) ratio is large. In this section, we derive a two-scalar model for a one-dimensional interface using a two-dimensional microstructure (Fig. 1). Similar to the model of [24], the model solves for the amount of scalar in phase i per total volume, denoted $c_i(x)$ for $i = 1, 2$. The total amount of scalar per total volume, $c_1(x) + c_2(x)$, is conserved. Since the diffuse interface is not in thermodynamic equilibrium, the local concentration values, denoted by $\tilde{c}_i(x, y)$ for $i = 1, 2$, are functions of both x and y in Fig. 1. The y-averaged mean concentration values within each finger are then denoted $\bar{\tilde{c}}_1(x) = c_1(x)/\phi(x)$ and $\bar{\tilde{c}}_2(x) = c_2(x)/(1 - \phi(x))$.

It is useful to illustrate that the model of [24] for a confined scalar (no interfacial transfer) is not only compatible with the proposed microstructure, but can be also derived from this approach. To show this, imagine that a scalar is confined to phase 1 in Fig. 1, or in other words, $D_2 = 0$. Then, the equation governing the amount of scalar per total volume, $c_1(x)$, is given by

$$\frac{\partial c_1}{\partial t} + \frac{\partial}{\partial x}(\vec{u}c_1) = \frac{\partial}{\partial x}\left(D_1\phi\frac{\partial \bar{\tilde{c}}_1}{\partial x}\right). \tag{8}$$

While the left hand side (LHS) terms represent the temporal and convective terms, the diffusive flux on the right hand side (RHS) of the first equality can be explained by considering the microstructure. Since there is no interfacial transfer across the sharp interfaces, the local concentration is only a function of x and the local diffusive flux is given by $D_1(\partial\bar{\tilde{c}}_1/\partial x)$. This flux has to then be weighted by the volume fraction of phase 1, $\phi(x)$, which results in the RHS term in Eq. (8). Due to the hyperbolic tangent profile of the diffuse interface at phase equilibrium, the relation

$$\nabla\phi = \frac{\phi(1-\phi)}{\epsilon}\vec{n} \tag{9}$$

holds, where $\vec{n} = \nabla\phi/|\nabla\phi|$ is the normal vector. Using this relation, and $\bar{\tilde{c}}_1(x) = c_1(x)/\phi(x)$, we can write the RHS in terms of known, resolved variables.

$$\frac{\partial c_1}{\partial t} + \frac{\partial}{\partial x}(\vec{u}c_1) = \frac{\partial}{\partial x}\left(D_1\phi\frac{\partial \bar{\tilde{c}}_1}{\partial x}\right) = \frac{\partial}{\partial x}\left[D_1\left(\frac{\partial c_1}{\partial x} - \frac{1-\phi}{\epsilon}\vec{n}c_1\right)\right]. \tag{10}$$

5.1. Scalar transfer model derivation

So far we have presented the derivation of the transport equation for a scalar confined to phase 1. A similar PDE can be derived for $c_2(x)$. In the general case when neither of the diffusivities are zero (finite D_1/D_2) the scalar is transferred between the phases. Here, we aim to derive the interfacial transfer terms that augment these PDEs to extend the work of [24] to arbitrary diffusivity ratios, D_1/D_2, and arbitrary jumps in equilibrium scalar concentrations across the interface, denoted K_{eq}. For heat transfer, $K_{\text{eq}} = (\rho_1 C_{p,1})/(\rho_2 C_{p,2})$, while $K_{\text{eq}} = H$, for mass transfer. We seek

the transfer terms denoted by $J(x)$ for

$$\frac{\partial c_1}{\partial t}+\frac{\partial}{\partial x}(\vec{u}c_1)=\frac{\partial}{\partial x}\left[D_1\left(\frac{\partial c_1}{\partial x}-\frac{1-\phi}{\epsilon}\vec{n}c_1\right)\right]+J(x), \tag{11}$$

$$\frac{\partial c_2}{\partial t}+\frac{\partial}{\partial x}(\vec{u}c_2)=\frac{\partial}{\partial x}\left[D_2\left(\frac{\partial c_2}{\partial x}+\frac{\phi}{\epsilon}\vec{n}c_2\right)\right]-J(x). \tag{12}$$

In order to close the model, $J(x)$ is to be determined in terms of known variables, as follows. The local concentration can be decomposed into a mean component and a perturbation, denoted by $\tilde{c}_i'(x,y)$ for $i=1,2$,

$$\tilde{c}_i(x,y)=\bar{\tilde{c}}_i(x)+\tilde{c}_i'(x,y). \tag{13}$$

Because of the assumed thin structure of the fingers in the microstructure, $h\ll\epsilon$, there is a quasi-steady balance between diffusion in x and y, yielding

$$\frac{\partial^2\tilde{c}_i'}{\partial y^2}=-\frac{\partial^2\bar{\tilde{c}}_i}{\partial x^2}, \tag{14}$$

for $i=1,2$. The thin structures are repeated periodically in the y direction with a period of $2h$. Let us focus on a half-period with thickness h, as shown in Fig. 1(c). Consider a coordinate system on the lower dashed line, then symmetry boundary conditions hold for phase 1 at $y=0$ and for phase 2 at $y=h$. Additionally, the perturbations have zero mean, i.e.,

$$\int_0^{\phi h}\tilde{c}_1'(x,y)dy=\int_{\phi h}^{h}\tilde{c}_2'(x,y)dy=0. \tag{15}$$

Integrating Eq. (14) twice in y and using the symmetry boundary conditions in addition to Eq. (15), we can determine the perturbations in terms of the mean concentrations to be given by

$$\tilde{c}_1'(x,y)=-\frac{1}{2}\left(\frac{\partial^2\bar{\tilde{c}}_1}{\partial x^2}\right)\left[y^2-\frac{(\phi h)^2}{3}\right], \tag{16}$$

$$\tilde{c}_2'(x,y)=-\frac{1}{2}\left(\frac{\partial^2\bar{\tilde{c}}_2}{\partial x^2}\right)\left\{(h-y)^2-\frac{[(1-\phi)h]^2}{3}\right\}. \tag{17}$$

Two other conditions must be satisfied at the sharp interface located at $y=\phi h$. First, thermodynamic equilibrium must be enforced, $\tilde{c}_1(x,y=\phi h)=K_{\mathrm{eq}}\tilde{c}_2(x,y=\phi h)$, which from Eqs. (16) and (17) results in

$$\phi^2\left(\frac{\partial^2\bar{\tilde{c}}_1}{\partial x^2}\right)-K_{\mathrm{eq}}(1-\phi)^2\left(\frac{\partial^2\bar{\tilde{c}}_2}{\partial x^2}\right)=\frac{3}{h^2}(\bar{\tilde{c}}_1-K_{\mathrm{eq}}\bar{\tilde{c}}_2). \tag{18}$$

Second, after plugging in Eqs. (16) and (17) to find the diffusive fluxes in the y direction, continuity of diffusive fluxes normal to the interface, $-D_1(\partial\bar{\tilde{c}}_1/\partial x)(\partial(\phi h)/\partial x)-D_1\partial\tilde{c}_1'/\partial y=-D_2(\partial\bar{\tilde{c}}_2/\partial x)(\partial(\phi h)/\partial x)-D_2\partial\tilde{c}_2'/\partial y$, results in

$$D_1\phi\left(\frac{\partial^2\bar{\tilde{c}}_1}{\partial x^2}\right)+D_2(1-\phi)\left(\frac{\partial^2\bar{\tilde{c}}_2}{\partial x^2}\right)=-D_1\frac{\partial\bar{\tilde{c}}_1}{\partial x}\frac{\partial\phi}{\partial x}+D_2\frac{\partial\bar{\tilde{c}}_2}{\partial x}\frac{\partial\phi}{\partial x}. \tag{19}$$

The interfacial transfer terms in Eqs. (11) and (12) are given by

$$J(x)=\frac{1}{h}D_1\left(\frac{\partial\tilde{c}_1'}{\partial y}\right)_{y=\phi h}-D_1\frac{\partial\bar{\tilde{c}}_1}{\partial x}\frac{\partial\phi}{\partial x}. \tag{20}$$

The first term on the RHS of Eq. (20) can be written in terms of $\partial^2\bar{\tilde{c}}_1/\partial x^2$ using Eq. (16). Invoking the sharp interface boundary conditions given by Eqs. (18) and (19), we can then find $\partial^2\bar{\tilde{c}}_1/\partial x^2$ and $\partial^2\bar{\tilde{c}}_2/\partial x^2$ in terms of lower-order derivatives. This results in

$$J(x)=\frac{1}{h^2}\frac{3D_1D_2}{K_{\mathrm{eq}}D_1(1-\phi)+D_2\phi}(K_{\mathrm{eq}}\bar{\tilde{c}}_2-\bar{\tilde{c}}_1)-K_{\mathrm{eq}}D_1(1-\phi)\frac{\partial\phi}{\partial x}\frac{-D_1\frac{\partial\bar{\tilde{c}}_1}{\partial x}+D_2\frac{\partial\bar{\tilde{c}}_2}{\partial x}}{K_{\mathrm{eq}}D_1(1-\phi)+D_2\phi}-D_1\frac{\partial\bar{\tilde{c}}_1}{\partial x}\frac{\partial\phi}{\partial x}. \tag{21}$$

The first term on the RHS of Eq. (21) originates from the diffusive flux in the y direction and has a very large $\mathcal{O}(1/h^2)$ prefactor. This term is indeed responsible for equilibrating the interface toward $\bar{\tilde{c}}_1(x)=K_{\mathrm{eq}}\bar{\tilde{c}}_2(x)$. The timescale for this equilibrium is proportional to h^2. Since h is an artificial free parameter in the assumed microscopic model that is chosen to be very small, we have freedom in the exact form of the first term in Eq. (21). The other terms on the RHS of this equation, however, are responsible for the correct prediction of long-time equilibrium solutions. As such, if we utilize $\bar{\tilde{c}}_1(x)=K_{\mathrm{eq}}\bar{\tilde{c}}_2(x)$ and the definitions of the mean concentration values, we can make the substitutions $\bar{\tilde{c}}_1=c_1+K_{\mathrm{eq}}c_2$ and $\bar{\tilde{c}}_2=c_1/K_{\mathrm{eq}}+c_2$ for these terms. After these substitutions and some algebraic simplifications, the final form of the transfer terms for a one-dimensional interface is

$$J(x)=AD_m[K_{\mathrm{eq}}c_2\phi-c_1(1-\phi)]-D_m\frac{\partial\phi}{\partial x}\frac{\partial(c_1+K_{\mathrm{eq}}c_2)}{\partial x}, \tag{22}$$

where D_m is the mixed diffusivity, given by

$$D_m=\frac{D_1D_2}{K_{\mathrm{eq}}D_1(1-\phi)+D_2\phi}. \tag{23}$$

Note that a new free parameter, A, is introduced in Eq. (22) in lieu of the prefactors in the first term on the RHS of Eq. (21). This free parameter represents the inverse time scale to thermodynamic equilibrium, typically chosen to be a large constant, without imposing additional time-step restrictions. Moreover, taking advantage of the aforementioned freedom in the form of the term responsible for equilibriating the interface, the first term on the RHS of Eq. (21) has been multiplied by $\phi(1-\phi)$, a kernel that is active in the interfacial region, such that it is in terms of the known variables, c_1 and c_2. This is also advantageous from a numerical perspective, as we avoid dealing with division by zero when evaluating $\bar{\tilde{c}}_i$ away from the interface. The final form of $J(x)$ in Eq. (22) is thus in terms of the known, conserved variables. The model was derived for a one-dimensional interface. The general model is then

$$\frac{\partial c_1}{\partial t}+\nabla\cdot(\vec{u}c_1)=\nabla\cdot\left[D_1\left(\nabla c_1-\frac{1-\phi}{\epsilon}\vec{n}c_1\right)\right]+AD_m[K_{\mathrm{eq}}c_2\phi-c_1(1-\phi)]-D_m\nabla\phi\cdot\nabla(c_1+K_{\mathrm{eq}}c_2), \tag{24}$$

$$\frac{\partial c_2}{\partial t}+\nabla\cdot(\vec{u}c_2)=\nabla\cdot\left[D_2\left(\nabla c_2+\frac{\phi}{\epsilon}\vec{n}c_2\right)\right]+AD_m[c_1(1-\phi)-K_{\mathrm{eq}}c_2\phi]+D_m\nabla\phi\cdot\nabla(c_1+K_{\mathrm{eq}}c_2). \tag{25}$$

A quick inspection of Eqs. 24 and 25 reveals satisfaction of some of the important model requirements enlisted in Section 3. Firstly, by summing the two equations, it becomes clear that the transfer terms cancel out resulting in a conservative transport equation for c_1+c_2, and therefore, c_1+c_2 is a conserved scalar. We have already explained generalizability of the model in terms of application to various diffuse interface methods and the capability of predicting both heat and mass transport. In terms of consistency, item (1) is satisfied because $D_m=0$ if one of the diffusivities is zero (see Eq. 23), resulting in zero interfacial transfer and reduction of the model to Eq. 10. Item (2) of the consistency requirements can also be observed from either of Eqs. 24 and 25. Let us consider Eq. 24 and the bulk of phase 1, i.e., ϕ tending

to 1. In this region of the domain, $1-\phi$, c_2 and $\nabla\phi$ all tend to zero, resulting in vanishing interfacial transfer, in addition to the diffusive flux reducing to $\nabla\cdot(D_1\nabla c_1)$, which matches the bulk equations presented in Section 2. In Section 6.1, by using canonical one-dimensional numerical tests, we demonstrate that the derived two-scalar model satisfies the remaining consistency requirements enlisted in Section 3. Afterwards, more practical multi-dimensional numerical simulations are presented in Section 6.2, where the scalar transport equation is coupled to the phase field and momentum transport equations, confirming accuracy, convergence, and positivity of the two-scalar model.

5.2. One-scalar model

Using the assumed microstructure and by assuming thermodynamic equilibrium at the interface, we can also derive a consistent one-scalar model for total species concentration/heat content per total volume. The interfacial transfer between the two phases need not be considered in the derivation of this model. By considering the contribution of each phase to the diffusive fluxes in a manner similar to the derivation of (10), and by invoking the thermodynamic equilibrium conditions, $\bar{c}_1(x) = K_{\text{eq}}\bar{c}_2(x)$, the derived one-scalar model for $c = c_1 + c_2$ is given by

$$\frac{\partial c}{\partial t} + \nabla\cdot(\vec{u}c) = \nabla\cdot\left[D_{\text{eff}}\nabla\left(\frac{c}{K_{\text{eff}}}\right)\right], \tag{26}$$

where

$$D_{\text{eff}} = D_1K_{\text{eq}}\phi + D_2(1-\phi), \tag{27}$$

and

$$K_{\text{eff}} = K_{\text{eq}}\phi + (1-\phi), \tag{28}$$

are the effective mixture diffusivity and equilibrium concentration ratio across interface, respectively. This model is introduced here as an alternative approach for modeling scalar transport, against which we compare the two-scalar model. For the sake of clarity, it is worth highlighting that for the case of heat transfer, solving Eqs (26)-(28) to find the heat content is equivalent to solving

$$\frac{\partial(\rho C_p)_{\text{eff}}T}{\partial t} + \nabla\cdot[\vec{u}(\rho C_p)_{\text{eff}}T] = \nabla\cdot(k_{\text{eff}}\nabla T) \tag{29}$$

to compute temperature, where

$$(\rho C_p)_{\text{eff}} = \rho_1C_{p,1}\phi + \rho_2C_{p,2}(1-\phi), \tag{30}$$

and

$$k_{\text{eff}} = k_1\phi + k_2(1-\phi), \tag{31}$$

are the effective mixture heat capacity and conductivity, respectively. Note that this one-scalar model is different from the one-scalar heat transfer model proposed by [17] in that it is in conservative form and in the way effective material properties are computed.

5.3. Computational approach

Numerically, we use a fourth-order Runge-Kutta (RK4) explicit scheme to time integrate Eqs. (24) and (25) coupled to Eq. (7). If solving for the flow field, we also couple these equations to the consistent momentum transport equations introduced in [33]. We use a second order central finite difference spatial discretization on a standard staggered Cartesian grid where velocity vectors and all fluxes, including the scalar fluxes, are stored on their respective faces, while pressure, density, viscosity, scalar concentrations and the phase field variable are stored on cell centers. If solving for momentum, we compute density and viscosity linearly with respect to the phase field variable, while surface tension forces are computed via the continuum surface force method. A block diagram summarizing the computational method is provided in Fig. 2. The interested reader can refer to [33] for a more detailed description of the computational algorithm (without scalar transport). The scalar transport step for the one-scalar and two-scalar models is straight-forward as it entails explicit time-advancement of an advection-diffusion-reaction equation spatially discretized with second order central differences.

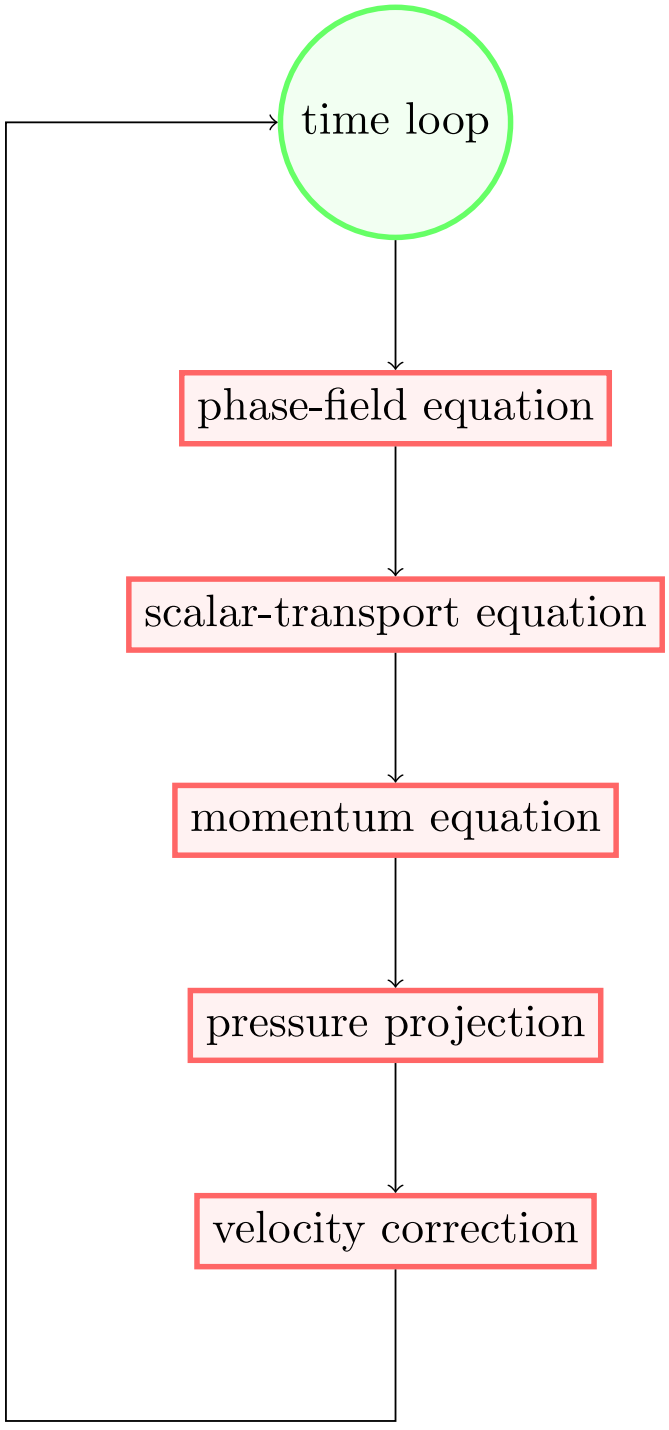

Fig. 2. A block diagram summarizing the computational steps involved in the fully coupled solver.

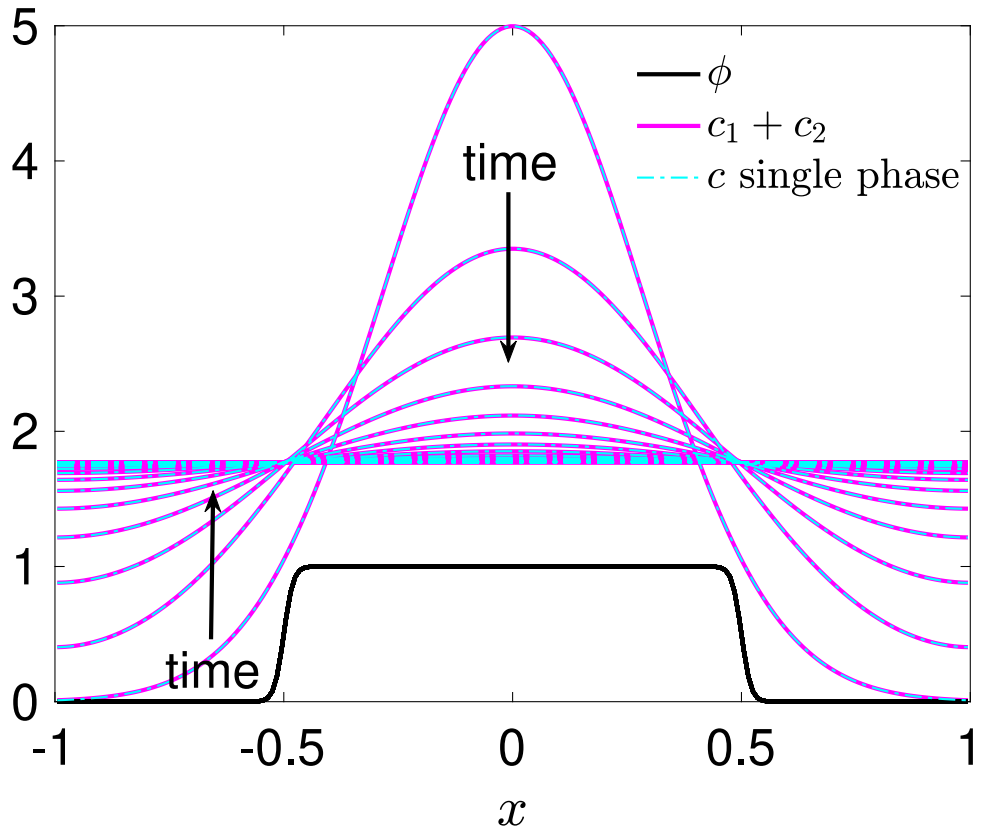

Fig. 3. Evolution of $c_1 + c_2$ from the two-scalar, two-phase model plotted on top of the solutions from a single-phase calculation at the same time instants. The drop, for the two-phase calculation, is denoted using the phase field profile.

5.4. Note on positivity

The scalar transport model in Eq. (10) with no interfacial transfer is guaranteed to maintain the positivity of scalar concentration, provided the constraint on grid cell size, Δx, given by

$$\Delta x \leq \frac{2D_1}{|\vec{u}|_{max}} \tag{32}$$

is satisfied [24] in addition to the Courant-Friedrichs-Lewy criterion for temporal stability [$\Delta t \leq \Delta x^2/(2D_f D_1)$, where D_f is the number of spatial dimensions, and Δt is the time step size]. This is sufficient to argue that the conserved quantity $c_1 + c_2$ in the two-scalar model remains positive with interfacial transfer. Note that, the transfer terms in Eqs. (24) and (25) cancel out identically. Therefore, as long as both c_1 and c_2 maintain positivity in the absence of transfer terms, i.e., $\Delta x \leq 2\min(D_1, D_2)/|\vec{u}|_{\max}$, the conserved quantity $c_1 + c_2$ is guaranteed to maintain positivity, even in the presence of transfer terms. Similarly, for the one-scalar model in Eq. (26), following the proof in [24] it can be shown that the positivity of the scalar concentration is guaranteed, provided the constraints $\Delta x \leq 2\min(D_1 K_{eq}, D_2)/[|\vec{u}|_{\max}\max(1, K_{eq})]$ and $\Delta t \leq \Delta x^2 \min(1, K_{eq})/[2D_f \max(D_1 K_{eq}, D_2)]$ are satisfied.

6. Numerical tests

In this section, we first present numerical simulation results that confirm the satisfaction of all the consistency requirements enlisted in Section 3 by the two-scalar model. While we explained in Section 5 that some of the requirements can be checked by inspecting the model, in Section 6.1 we use 1D tests to numerically demonstrate that the consistency requirements (3)-(5) presented in Section 3 are met. More complex, multidimensional cases where the scalar transport is solved in conjunction with the Navier-Stokes equation are presented in Section 6.2. All numerical tests are performed in dimensionless form unless physical units are specified.

6.1. One-dimensional tests

All the simulations presented in this section are one dimensional in nature and static. For all the simulations, the domain is chosen to be $[-1, 1]$, the grid cell size is $\Delta x = 0.01$, and the parameters are taken to be $\epsilon = 0.01$, $\gamma = 1$, and $A = 1000$. Note that ϵ and γ are chosen based on the boundedness criterion established in [31], while A, representing the inverse time scale to thermodynamic equiibrium is chosen to be a large constant while not reducing the time-step requirements.

6.1.1. Equivalence to single phase when $D_1 = D_2, K_{eq} = 1$

If the diffusivities on the two sides of the interface are equal, then the presence of the interface should have no effect on the transport of the scalar throughout the domain, thereby effectively reducing the problem setup to a pseudo-single-phase problem [consistency item (3) in Section 3]. Here, we numerically verify this consistency for the two-scalar model. In particular, we set $D_1 = D_2 = K_{eq} = 1$ and use periodic boundary conditions to study the evolution of the system starting from $c_1(x, t = 0) = 5\exp(-4x^2)\phi$, $c_2(x, t = 0) = 5\exp(-4x^2)(1 - \phi)$, while the artificial drop has a diameter of 1 and is placed in the center of the domain. Fig. 3 shows that as the scalar diffuses towards a flat solution, the solutions predicted by the two-scalar, two-phase model match very well with the numerical solutions from a single-phase calculation with the same resolution and discretization.

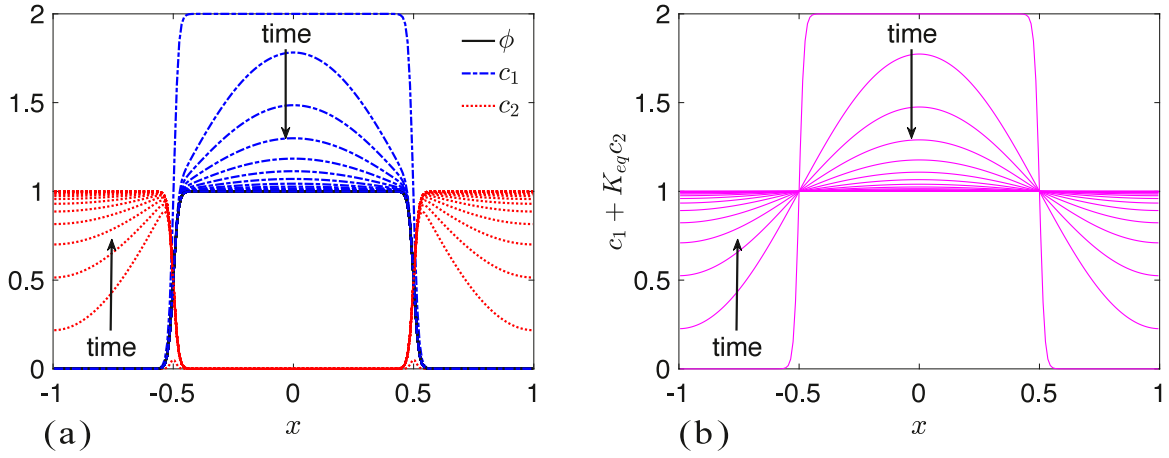

Fig. 4. The evolution of (a) c_1 and c_2 plotted on top of the drop profile given by ϕ and (b) $c_1 + K_{eq}c_2$ plotted for simulations performed with $D_1 = D_2 = K_{eq} = 1$.

6.1.2. Flat equilibrium solutions

A one-dimensional drop of phase 1 with diameter 1 is placed in the middle of the domain. The initial conditions are $c_1(x, t = 0) = 2\phi(x, t = 0)$ and $c_2(x, t = 0) = 0$ and we use periodic boundary conditions. The equilibrium solution is expected to be flat profiles within the drop and outside it with a jump based on the value of K_{eq}. In particular, $c_1 + K_{eq}c_2$ should be a flat profile at equilibrium.

In Fig. 4(a), the evolution of c_1 and c_2 are plotted on top of the drop profile for a simulation performed using $D_1 = D_2 = K_{eq} = 1$. In Fig. 4(b), at the same time instants, values of $c_1 + K_{eq}c_2 = c_1 + c_2$ are plotted, showing the correct flat profile at equilibrium.

In Fig. 5, for the same initial conditions and boundary conditions, simulation results for $K_{eq} = 1/3$ are illustrated. Fig. 5(a,b) demonstrate how c_1, c_2 and $c_1 + K_{eq}c_2$ evolve in time for $D_1 = D_2 = 1$. Exploring the effect of the diffusivity ratio, Fig. 5(c,d) demonstrate the evolution of c_1, c_2 and $c_1 + K_{eq}c_2$ for $D_1 = 10, D_2 = 1$. Finally, Fig. 5(d,e) serve the same purpose for $D_1 = 1, D_2 = 10$. It is clear from comparing Fig. 5(c) and (e) that the scalar diffuses much faster in the phase with the higher diffusivity, resulting in flat profiles within phase 1 and 2 in Fig. 5(c) and (e), respectively.

6.1.3. Linear equilibrium solutions

A one-dimensional drop of phase 1 with radius 1 is placed on the right half of the domain. The initial conditions are again $c_1(x, t = 0) = 2\phi(x, t = 0)$ and $c_2(x, t = 0) = 0$ and we use Dirichlet boundary conditions given by $c_1(x = -1, t) = c_2(x = -1, t) = 0$ and $c_1(x = 1, t) = 2, c_2(x = 1, t) = 0$. The equilibrium solutions are expected to be linear profiles within the drop and outside it, with slopes that are inversely proportionate to the diffusivity in each phase and a jump in accordance with the value of K_{eq}. In this case, $c_1 + K_{eq}c_2$ should consist of two lines with no jump across the interface at equilibrium.

In Fig. 6(a), the evolution of c_1 and c_2 are plotted on top of the drop profile for a simulation performed using $D_1 = D_2 = K_{eq} = 1$. In Fig. 6(b), $c_1 + K_{eq}c_2 = c_1 + c_2$ is plotted at the same time instants, showing the correct linear profile at equilibrium. We vary the diffusivity ratio, $D_1 = 10, D_2 = 1$, in the next simulation, shown in Fig. 6(c,d). For this case, the behavior of the solution is not monotonic with time in the phase with higher diffusivity. Finally, going back to $D_1 = D_2 = 1$, we test the effect of varying the interfacial jump, $K_{eq} = 1/3$, as depicted in Fig. 6(e,f).

It must be emphasized that while the tests presented in this section might seem to have trivial solutions, the correct prediction of these solutions depends on the details of the two-scalar model presented in Eqs. (24) and (25). In particular, if the last transfer term in these equations were to be excluded or altered, the equilibrium solutions would be grossly mispredicted.

6.1.4. Large diffusivity ratios

As mentioned in Section 2.2, a very important limit for which we need the solutions from our models to be accurate is at large diffusivity ratios.Jain and Mani [24] showed that the model presented in Eq. (10) prevents leakage for a confined scalar (e.g., $D_2 = 0$), whereas the naive one-scalar model presented in Section 5.2 results in significant leakage to the phase with zero diffusivity. As explained in Section 5, our two-scalar model [Eq. (24)] reduces to the confined scalar model in Eq. (10) when one of the diffusivities is zero, i.e., the scalar is confined (consistency item (1) in Section 3). However, an important limit we study numerically here is large but finite diffusivity ratios to show that the derived two-scalar model satisfies consistency item (5) in Section 3. Fig. 7 compares the performance of the two-scalar model against the one-scalar model for $D_1 = 1$, $D_2 = 10^{-4}$, $K_{eq} = 1$. For the two-scalar model the initial conditions are $c_1(x, t = 0) = \phi$, $c_2(x, t = 0) = 0$, whereas for the one-scalar model the simulations are initialized with $c(x, t = 0) = \phi$. Fig. 7 compares the simulation results from the two-scalar model [Fig. 7(a)] against those from the one-scalar model [Fig. 7(b)] for the same time instants from $t = 0$ to $t = 1$. For such a short time interval, since D_2 is so small, the scalar should essentially all remain inside phase 1. The results from the two-scalar model are in agreement with this expectation; whereas, the one-scalar model results suffer from significant artificial leakage into phase 2.

6.2. Multi-dimensional tests

Using the preceding numerical tests, we numerically demonstrated that the two-scalar model satisfies the consistency requirements (3)-(5) from Section 3. In the following, we demonstrate the accuracy and convergence properties of the developed two-scalar model on a few more practical problems. In the following tests, similar to the 1D tests in Section 6.1, we use $A = 1000$, $\epsilon = \Delta x$, and $\gamma = |\vec{u}|_{\max}$.

6.2.1. Bubble depletion

We adopt a three-dimensional test from [18], in which we are interested in predicting dispersed-phase diffusion control from a bubble into its surrounding phase. This circumstance arises when $K_{\text{eq}} \ll 1$, corresponding to, for instance, heat transfer from a bubble with much lower heat capacity than its background. Specifically,

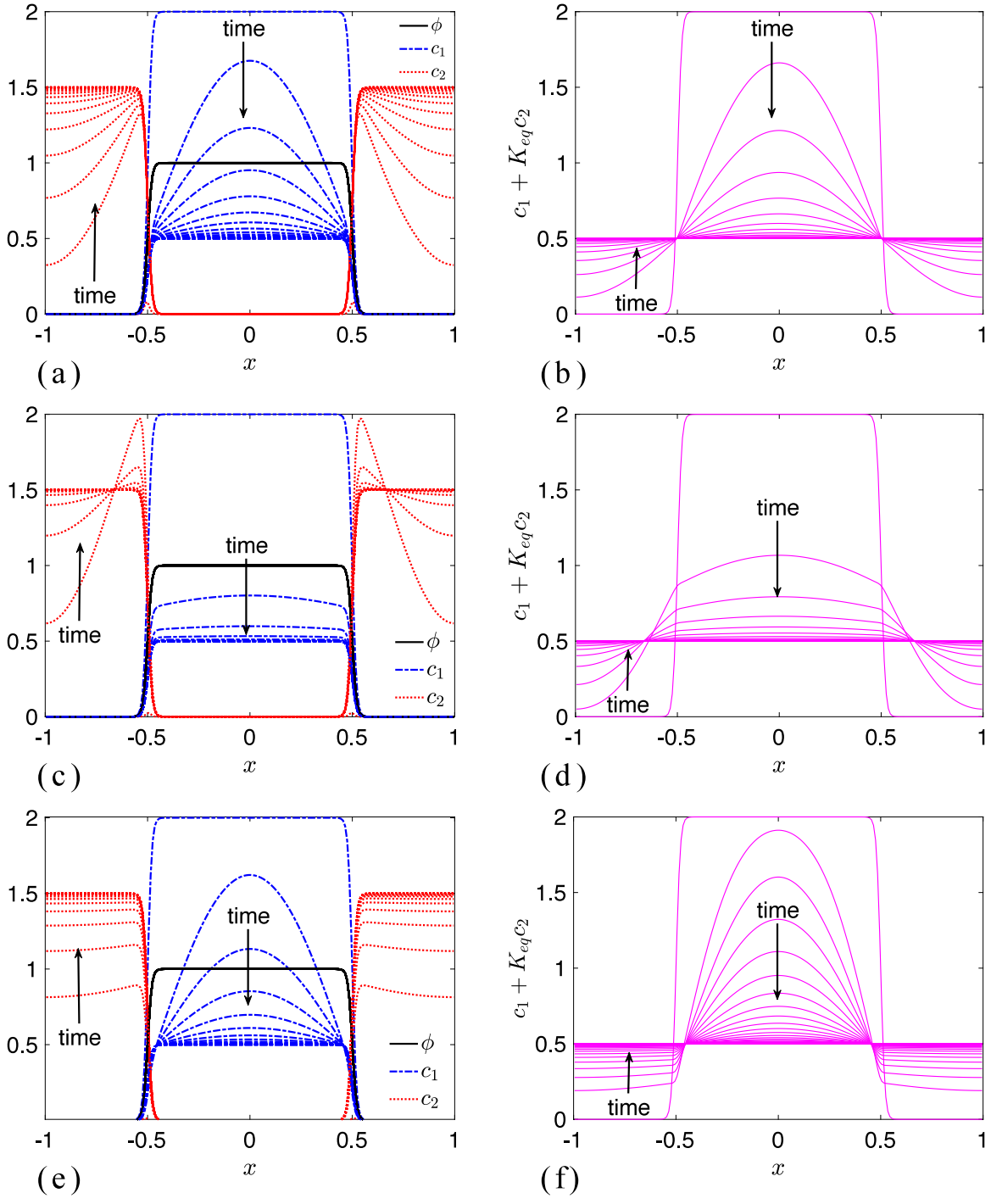

Fig. 5. For jump conditions given by $K_{eq} = 1/3$, the evolution of (a) c_1 and c_2 plotted on top of the drop profile given by ϕ and (b) $c_1 + K_{eq}c_2$ plotted for simulations performed with $D_1 = D_2 = 1$, (c) c_1 and c_2 plotted on top of the drop profile given by ϕ and (d) $c_1 + K_{eq}c_2$ plotted for simulations performed with $D_1 = 10, D_2 = 1$ and (e) c_1 and c_2 plotted on top of the drop profile given by ϕ and (f) $c_1 + K_{eq}c_2$ plotted for simulations performed with $D_1 = 1, D_2 = 10$.

we are interested in predicting the evolution of the heat content in a two-phase system consisting of a bubble with radius $R = 0.32$ of phase 1 in a $1 \times 1 \times 1$ domain otherwise filled with fluid of phase 2. We set $D_1 = 3.62 \times 10^{-4}$, $D_2 = 3.62 \times 10^{-9}$, $K_{eq} = 10^{-5}$, and perform simulations with the two-scalar and one-scalar models. Periodic boundary conditions are used and the heat content is initialized to be $q_1(\vec{x}, t = 0) = \phi$, $q_2(\vec{x}, t = 0) = 0$ for the two-scalar model and consistently, we set $q_{os}(\vec{x}, t = 0) = \phi$ for the one-scalar model, where subscript os stands for one scalar. Theoretically, since K_{eq} is very small, $q_1 \approx 0$ at the interface for $t > 0$. As such, heat continues to diffuse from inside of the bubble to its interface and is then transferred to the surrounding phase. Moreover, because $D_1 \gg D_2$, while heat is leaving the bubble, it is mostly accumulated around the interface in phase 2 because it diffuses to the regions away from the bubble with a much slower rate. Fig. 8 shows how the heat content in each phase evolves in time and space. Specifically, from a simulation with a $100 \times 100 \times 100$ mesh, panels (a), (b), and (c) show the heat content solutions from both models as a function of x with $y = z = 0.5$ for times of $t = 13.33$, $t = 40$, and $t = 80$, respectively. Panel (d) shows the long time state of the so-

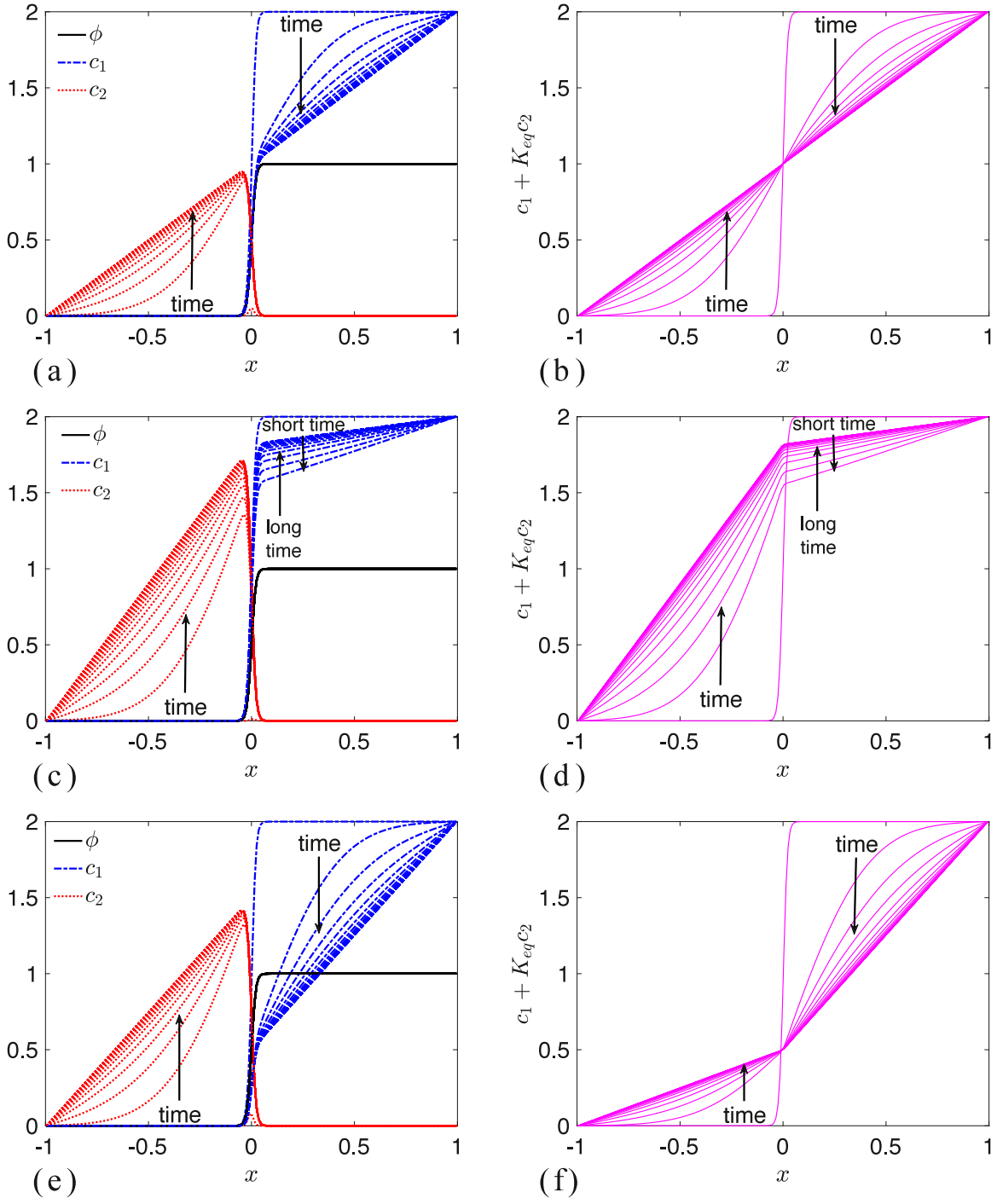

Fig. 6. The evolution of (a) c_1 and c_2 plotted on top of the drop profile given by ϕ and (b) $c_1 + K_{eq}c_2$ plotted for simulations performed with $D_1 = D_2 = K_{eq} = 1$, (c) c_1 and c_2 plotted on top of the drop profile given by ϕ and (d) $c_1 + K_{eq}c_2$ plotted for simulations performed with $D_1 = 10, D_2 = K_{eq} = 1$ and (e) c_1 and c_2 plotted on top of the drop profile given by ϕ and (f) $c_1 + K_{eq}c_2$ plotted for simulations performed with $D_1 = D_2 = 1, K_{eq} = 1/3$.

lution at $t = 250$, when $q_1 \approx 0$ everywhere, and all the heat has been transferred from the bubble to the surrounding phase. Qualitatively, by comparing the value of $q_1 + q_2$ from the two-scalar model against q_{os} from the one-scalar model, we can observe that the two-scalar model indeed allows for the heat to be transferred to the surrounding phase whereas the one-scalar model seems to retain the heat inside the bubble, which is unphysical.

A more quantitative comparison is presented in Fig. 9, where we plot the predicted heat content in the bubble as a function of time from the two-scalar model, $Q = \int q_1 dV$, and the one-scalar model, $Q_{os} = \int q_{os} K_{eq}\phi/(1 - \phi + K_{eq}\phi) dV$, against the theoretical solution [18,36]. As the mesh is refined with $\epsilon = \Delta x$, it is clear that the two-scalar model converges to the exact solution. In contrast, the one-scalar model seems to predict solutions that do not converge to the exact solution and have errors that are more than an order of magnitude larger than the two-scalar model. For comparison, we have included the predictions of the two-scalar sharp-interface model of [18] using a $100 \times 100 \times 100$ grid, showing that

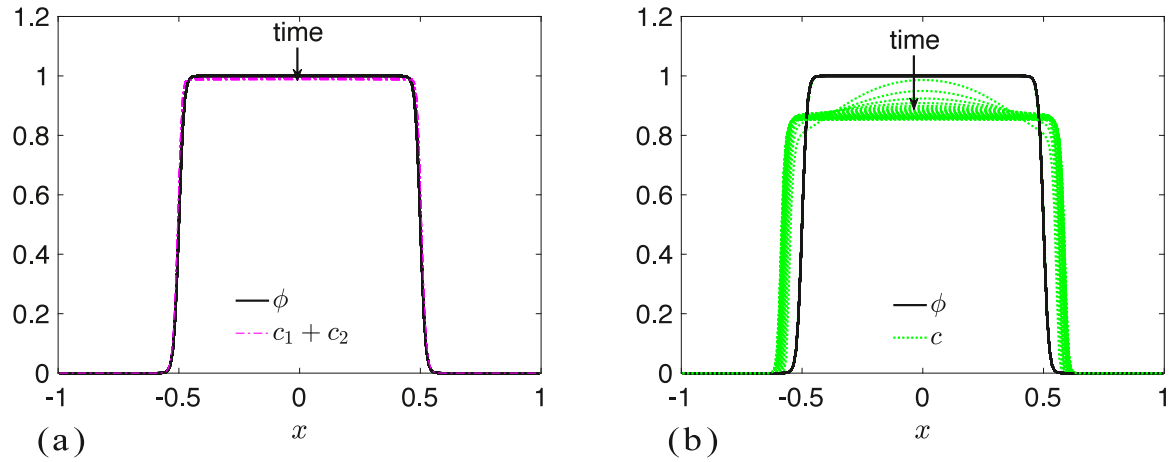

Fig. 7. Evolution of the scalar field up to $t = 1$ plotted for $D_1 = 1$, $D_2 = 10^{-4}$, $K_{eq} = 1$ using (a) the two-scalar model given in Eqs. (24),(25) and (b) the one-scalar model given in Eq. (26).

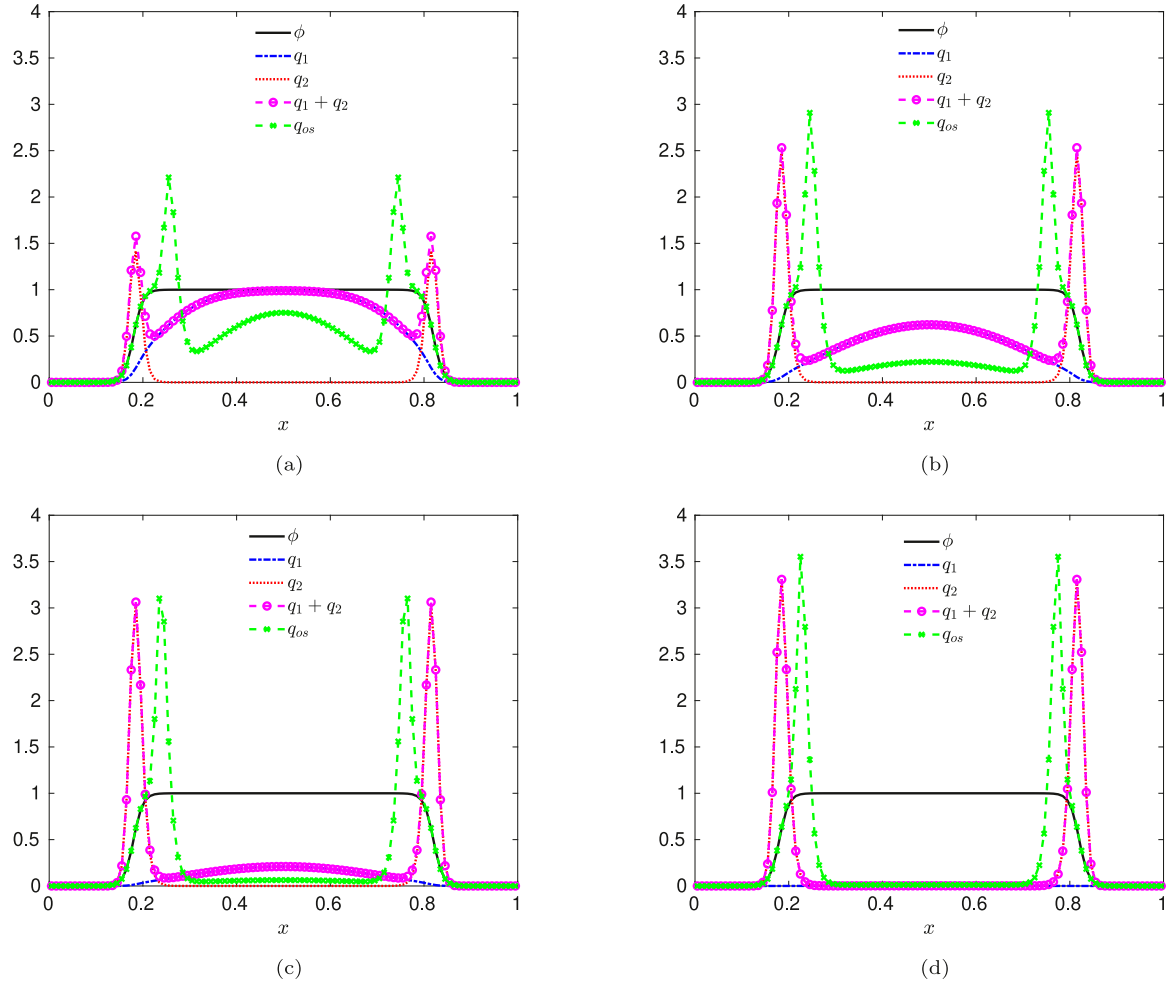

Fig. 8. The predicted spatial distribution of heat content (in either phase and total) on the line of $y = z = 0.5$ from simulations on a $100 \times 100 \times 100$ grid using the two-scalar model compared against the one scalar model at times (a) $t = 13.33$, (b) $t = 40$, (c) $t = 80$, and (d) $t = 250$.

indeed our proposed two-scalar model is more accurate. Note here, the y-axis is plotted in log scale, which clearly differentiates the errors in the models. However, the results in the literature [18,37] are typically plotted in linear scale, which makes it difficult to quantify the accuracy of such models.

6.2.2. Rising bubble

A two-dimensional test involving dilute mass transfer of oxygen from a rising air bubble (phase 2) to an initially stationary background of liquid water (phase 1) is adopted from [21]. The air bubble has a diameter of $d_B = 1$ mm, and rises due to buoyancy forces

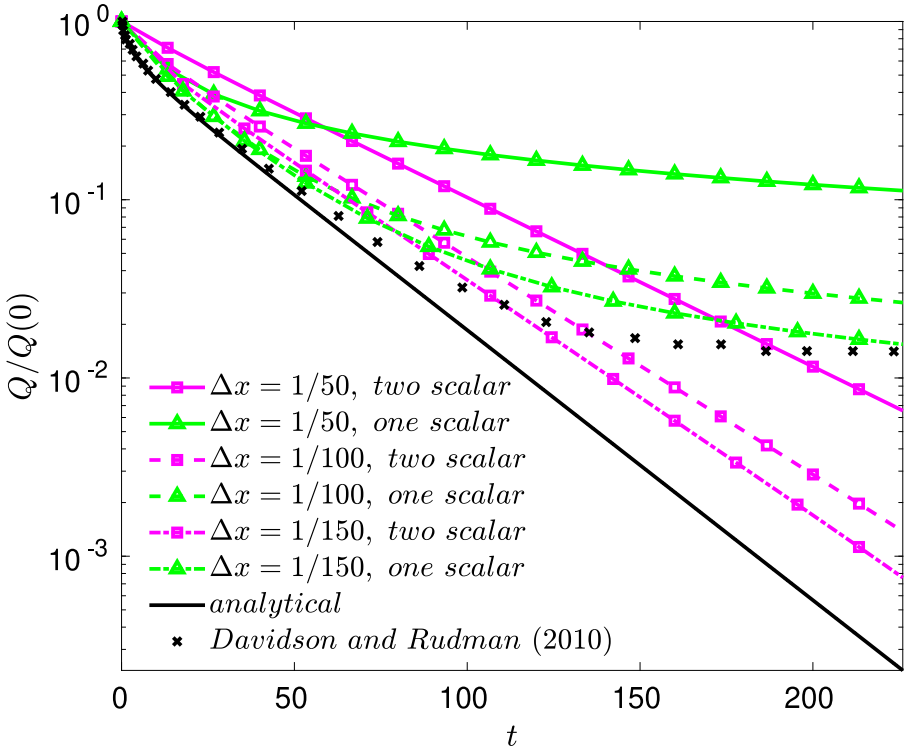

Fig. 9. Predicted temporal evolution of heat content in the bubble of phase 1 from simulations at various resolutions using the one-scalar and two-scalar models shown in comparison to the analytical solution and results of [18] using a sharp-interface two-scalar model with $\Delta x = 1/100$.

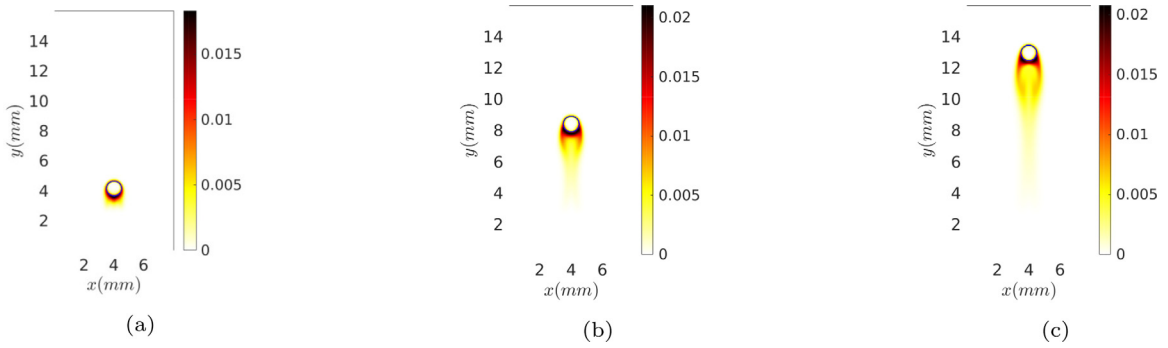

Fig. 10. Predicted concentration of dissolved oxygen in water (c_1) for the rising bubble case using the two-scalar model on a 192×384 mesh at (a) $t = 0.0209$s, $t = 0.0628$s, and 0.104s, plotted on top of the interface position given by the $\phi = 0.5$ contour lines.

with $g = 9.8$ m/s^2. The Henry coefficient is $K_{eq} = 1/33$, corresponding to oxygen diffusion in air/water systems at standard conditions. The material properties are $\rho_1 = 1000$ kg/m^3, $\rho_2 = 1.2$ kg/m^3, $\mu_1 = 1 \times 10^{-2}$ Pa s, $\mu_2 = 1.8 \times 10^{-5}$ Pa s, $D_1 = 10^{-6}$ m^2/s, and $D_2 = 5 \times 10^{-6}$ m^2/s. All material properties are realistic, except for liquid viscosity which is chosen to be higher than that of water, corresponding to a Schmidt number of $Sc = \nu/D = 10$. This increases the thickness of the hydrodynamic boundary layer, allowing for employment of relatively coarse grids. The domain is 8 mm $\times$ 16 mm, with slip boundary conditions on all walls and Neumann boundary conditions for all scalars. The drop is initially placed at (4 mm, 3 mm), with $c_1(\vec{x}, t = 0) = 0$, $c_2(\vec{x}, t = 0) = 1 - \phi$ for the two-scalar model and consistently, we set $c_{os}(\vec{x}, t = 0) = 1 - \phi$ for the one-scalar model. In Fig. 10, we present the predicted dissolved oxygen concentration in water (c_1) at times $t =$ 0.0209 s, 0.0628 s, 0.104 s for two-scalar model simulations on a 192×384 mesh.

A more quantitative assessment of accuracy is provided in Fig. 11. We present the predicted normalized mass of oxygen inside the bubble as a function of dimensionless time, t/τ, where $\tau = d_B/u_{rise} = 0.013$ s. Results from the two-scalar and one-scalar models are compared at three different resolutions against the high resolution (512×1024), mesh-converged numerical results of the sharp-interface method of [21]. It is clear that while the two-scalar model predictions are converging to the solutions of [21], the one-scalar model sustains very large errors that can be especially problematic for simulations of bubbly flows with many bubbles.

6.2.3. Gas transfer in breaking waves

In this section, a two-dimensional simulation of gas transfer in a breaking wave is presented as a proof of concept of applicability of the proposed two-scalar model for realistic simulations. The parameters used in this simulation are: $\rho_1 = 1$,

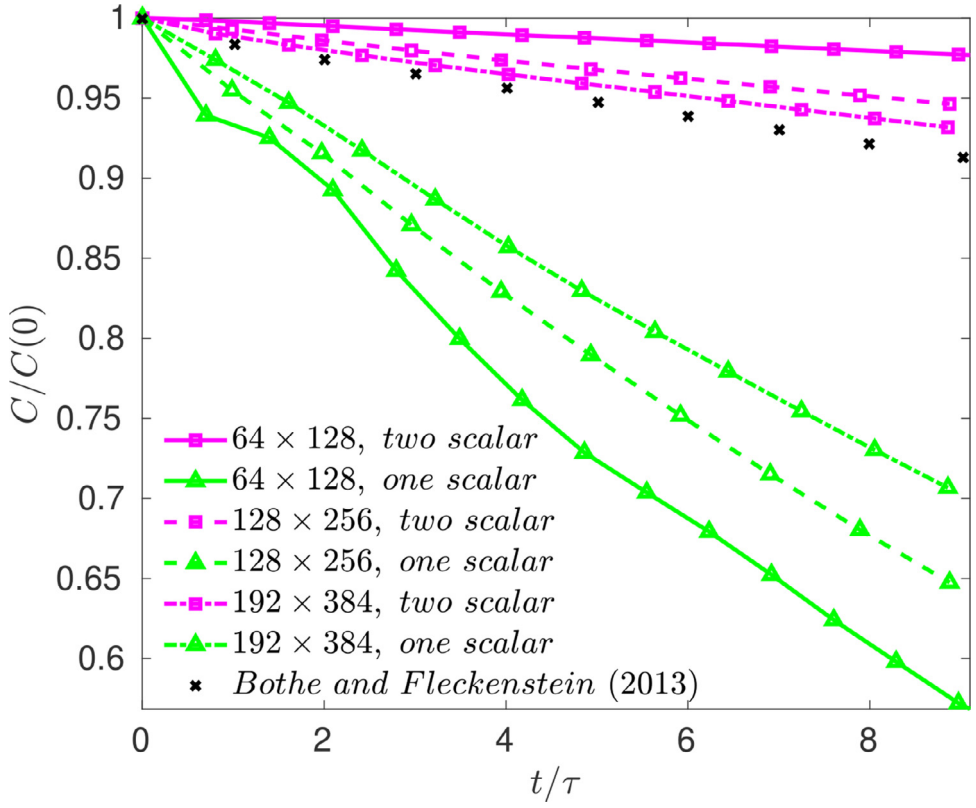

Fig. 11. Predicted temporal evolution of normalized oxygen mass in bubble of phase 2 from simulations at various resolutions using the one-scalar and two-scalar models shown in comparison to the high resolution (512×1024), mesh-converged numerical solutions of [21].

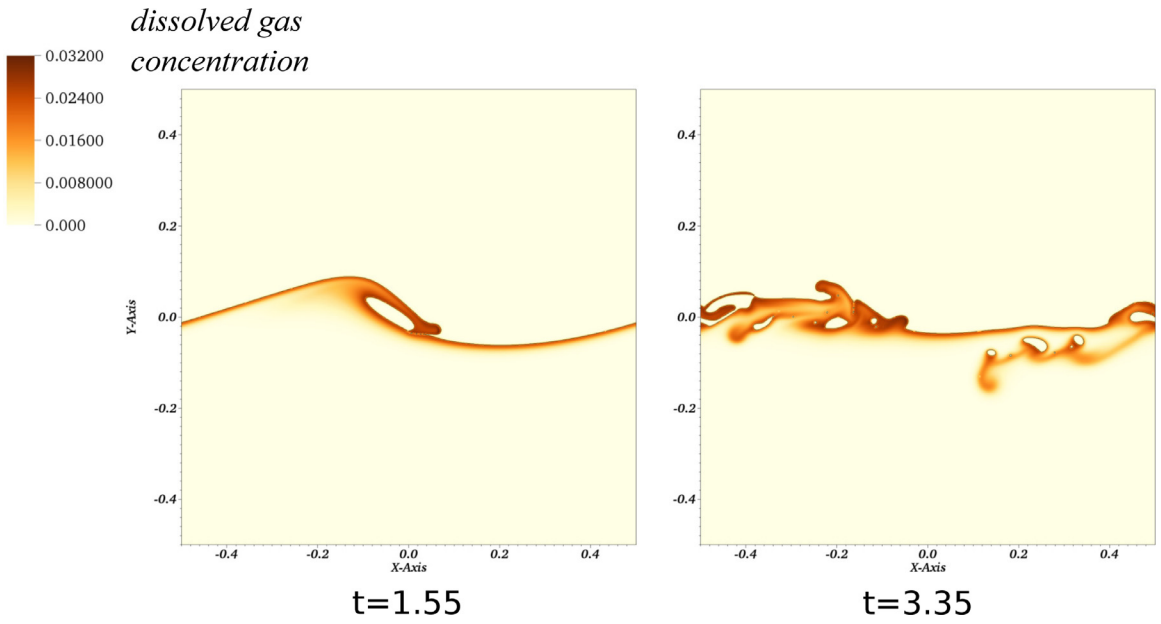

Fig. 12. Snapshots depicting a two-dimensional breaking wave with gas transfer across the interface at two time instances of t = 1.55 and t = 3.35. The colors show the dissolved scalar concentration (c_2) as a function of space and time.

$\rho_2 = 10^2$, $\mu_1 = 4 \times 10^{-3}$, $\mu_2 = 10^{-2}$, $D_1 = 4 \times 10^{-3}$, $D_2 = 10^{-4}$, and $K_{eq} = 33$.

The initial setup of the breaking wave corresponds to a Stokes wave from the work of [38]. The dissolved gas is initially assumed to be uniformly distributed in phase 1, i.e., the initial value of $c_1 = \phi$ and $c_2 = 0$. A grid of 1024×1024 is used to compute a highly resolved simulation. The snapshots from the simulation at two different time instances are shown in Fig. 12 showing the dissolved gas concentration (c_2). A grid convergence study is also presented using three grids of sizes 256×256, 512×512, and 1024×1024 and the results in terms of total amount of scalar dissolved in phase 2 as a function of time is shown in Fig. 13. It is clear from Figs. 12 and 13 that as the breaking wave entrains bubbles, there is an increase in the amount of dissolved scalar within the liquid phase. Moreover, Fig. 12 shows that due to the relative small diffusivity of phase 2, most of

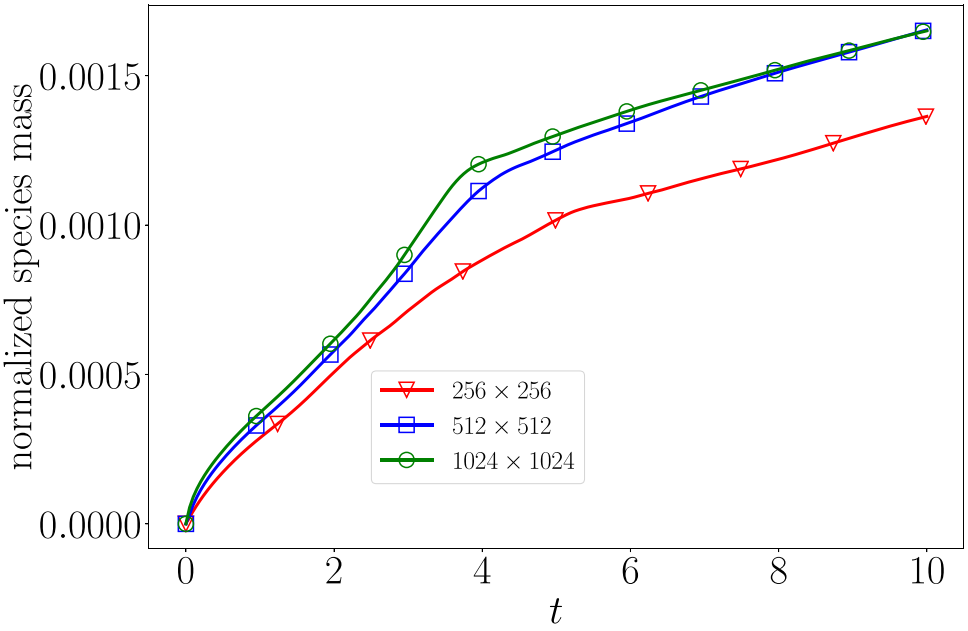

Fig. 13. The total amount of scalar dissolved in phase 2 as a function of time for three different grid resolution simulations of the two-dimensional breaking wave.

the dissolved gas remains close to the interfacial regions of the flow.

7. Conclusions

Second-order conservative phase field (diffuse interface) models offer desirable advantages compared to sharp-interface models such as VOF and LS, and avoid some of the PDE-level issues associated with diffuse interface models based on the Cahn-Hilliard equation. In this work, we derived an interfacial scalar transfer model that can be used to consistently model heat and mass transfer between immiscible phases in conjunction with second order conservative phase field models. Specifically, by assuming an interface microstructure that is consistent with the interfacial profile of phase field methods, we anaytically applied the sharp interface equations within the microscopic structure to derive the upscaled equations governing conserved scalars such as heat content or dilute species concentration for diffuse interfaces. The resulting two-scalar model for heat/mass transfer can be applied to arbitrary diffusivity ratios and jump conditions. Assuming thermodynamic equilibrium at the interface, we also derived a consistent one-scalar model for conserved scalars which was primarily utilized here to demonstrate the advantages of using the two-scalar model. Using theoretical arguments and one-dimensional tests we demonstrated that the two-scalar model satisfies important consistency properties in the sense of (1) reducing to the confined scalar model [24] when diffusivity is zero in one of the phases, (2) reducing to the bulk equations away from the interface, (3) converging to a single-phase calculation when the two phases are identical, (4) predicting equilibrium profiles accurately in various limits, and (5) preventing leakage in the practical limit of large diffusivity ratios. Additionally, we presented three practical problems in two-dimensional and three-dimensional settings, involving heat transfer from a stationary bubble, mass transfer from a rising bubble and gas transfer in a breaking wave. We showed that for practical scenarios with large diffusivity ratios or large K_{eq} (i.e., heat capacity ratio or Henry's constant) values, the two-scalar model provides much more accurate results compared to the alternative one-scalar model, in addition to converging to the correct results at relatively low resolutions.

Declaration of Competing Interest

The authors declare that they have no known competing financial interests or personal relationships that could have appeared to influence the work reported in this paper.

CRediT authorship contribution statement

Shahab Mirjalili: Methodology, Formal analysis, Resources, Software, Visualization, Investigation, Data curation, Writing – original draft, Validation. **Suhas S. Jain:** Investigation, Data curation, Formal analysis, Writing – review & editing. **Ali Mani:** Conceptualization, Supervision, Writing – review & editing.

Acknowledgements

This material is based upon work supported by the Defense Advanced Research Projects Agency (DARPA) under agreement No. HR00112090065. The authors thank Changxiao Shao for helpful comments on an early draft of this manuscript. Additionally, S. S. J. acknowledges discussions with Parviz Moin and Ronald Chan on simulation of breaking waves.

References

[1] T. Nomura, M. Tsubota, T. Oya, N. Okinaka, T. Akiyama, Heat storage in direct-contact heat exchanger with phase change material, Appl. Therm. Eng. 50 (2013) 26–34.
[2] H.Z. Kister, J.R. Haas, D.R. Hart, D.R. Gill, Distillation Design, 1, McGraw-Hill, New York, 1992.
[3] F.A. Williams, Combustion Theory, CRC Press, 2018.
[4] A.H. Lefebvre, V.G. McDonell, Atomization and Sprays, CRC press, 2017.
[5] N. Kantarci, F. Borak, K.O. Ulgen, Bubble column reactors, Process Biochem. 40 (2005) 2263–2283.
[6] D. Orlebeke, J.K. Orlebeke, Oxygenation of aqueous systems, 2009. US Patent App. 11/917,746.
[7] T. Stephenson, K. Brindle, S. Judd, B. Jefferson, Membrane Bioreactors for Wastewater Treatment, IWA publishing, 2000.
[8] R. Lal, Carbon sequestration, Philos. Trans. R. Soc. Lond. B Biol. Sci. 363 (2008) 815–830.
[9] S. Mirjalili, S.S. Jain, M. Dodd, Interface-capturing methods for two-phase flows: an overview and recent developments, center for turbulence research annual research briefs (2017) 117–135.
[10] S. Mirjalili, C.B. Ivey, A. Mani, Comparison between the diffuse interface and volume of fluid methods for simulating two-phase flows, Int. J. Multiph. Flow 116 (2019) 221–238.

[11] D. Bothe, M. Koebe, K. Wielage, J. Prüss, H.-J. Warnecke, Direct numerical simulation of mass transfer between rising gas bubbles and water, in: Bubbly Flows, Springer, 2004, pp. 159–174.
[12] V. Mehdi-Nejad, J. Mostaghimi, S. Chandra, Modelling heat transfer in two-fluid interfacial flows, Int. J. Numer. Methods Eng. 61 (2004) 1028–1048.
[13] D. Deising, D. Bothe, H. Marschall, Direct numerical simulation of mass transfer in bubbly flows, Comput. Fluids 172 (2018) 524–537.
[14] C. Yang, Z.-S. Mao, Numerical simulation of interphase mass transfer with the level set approach, Chem. Eng. Sci. 60 (2005) 2643–2660.
[15] J. Wang, P. Lu, Z. Wang, C. Yang, Z.-S. Mao, Numerical simulation of unsteady mass transfer by the level set method, Chem. Eng. Sci. 63 (2008) 3141–3151.
[16] N. Balcázar-Arciniega, O. Antepara, J. Rigola, A. Oliva, A level-set model for mass transfer in bubbly flows, Int. J. Heat Mass Tran. 138 (2019) 335–356.
[17] X. Zheng, H. Babaee, S. Dong, C. Chryssostomidis, G. Karniadakis, A phase-field method for 3D simulation of two-phase heat transfer, Int. J. Heat Mass Trans. 82 (2015) 282–298.
[18] M.R. Davidson, M. Rudman, Volume-of-fluid calculation of heat or mass transfer across deforming interfaces in two-fluid flow, Numer. Heat Trans. B-Fund. 41 (2002) 291–308.
[19] A. Alke, D. Bothe, M. Kroeger, H. Warnecke, VOF-based simulation of conjugate mass transfer from freely moving fluid particles (2009) 157–168.
[20] H. Marschall, K. Hinterberger, C. Schüler, F. Habla, O. Hinrichsen, Numerical simulation of species transfer across fluid interfaces in free-surface flows using OpenFOAM, Chem. Eng. Sci. 78 (2012) 111–127.
[21] D. Bothe, S. Fleckenstein, A volume-of-fluid-based method for mass transfer processes at fluid particles, Chem. Eng. Sci. 101 (2013) 283–302.
[22] S. Fleckenstein, D. Bothe, A volume-of-fluid-based numerical method for multi-component mass transfer with local volume changes, J. Comput. Phys. 301 (2015) 35–58.
[23] J. Berry, M. Davidson, D.J. Harvie, A multiphase electrokinetic flow model for electrolytes with liquid/liquid interfaces, J. Comput. Phys. 251 (2013) 209–222.
[24] S.S. Jain, A. Mani, Modeling transport of scalars in two-phase flows with a diffuse-interface method, arXiv preprint arXiv:2011.10705(2020).
[25] J.C. Slattery, Advanced Transport Phenomena, Cambridge University Press, 1999.
[26] M. Ishii, T. Hibiki, Thermo-fluid Dynamics of Two-phase Flow, Springer Science & Business Media, 2010.
[27] S.M. Allen, J.W. Cahn, A microscopic theory for antiphase boundary motion and its application to antiphase domain coarsening 27(1979) 1085–1095.
[28] Y. Sun, C. Beckermann, Sharp interface tracking using the phase-field equation, J. Comput. Phys. 220 (2007) 626–653.
[29] Z. Huang, G. Lin, A.M. Ardekani, Consistent and conservative scheme for incompressible two-phase flows using the conservative Allen-Cahn model, J. Comput. Phys. 420 (2020) 109718.
[30] P.-H. Chiu, Y.-T. Lin, A conservative phase field method for solving incompressible two-phase flows, J. Comput. Phys. 230 (2011) 185–204.
[31] S. Mirjalili, C.B. Ivey, A. Mani, A conservative diffuse interface method for two-phase flows with provable boundedness properties, J. Comput. Phys. 401 (2020) 109006.
[32] S.S. Jain, Accurate conservative phase-field method for simulation of two-phase flows, arXiv preprint arXiv:2203.05802(2022).
[33] S. Mirjalili, A. Mani, Consistent, energy-conserving momentum transport for simulations of two-phase flows using the phase field equations, J. Comput. Phys. (2020) 109918.
[34] P. Yue, C. Zhou, J.J. Feng, Spontaneous shrinkage of drops and mass conservation in phase-field simulations, J. Comput. Phys. 223 (2007) 1–9.
[35] S.S. Jain, A. Mani, P. Moin, A conservative diffuse-interface method for compressible two-phase flows, J. Comput. Phys. (2020) 109606.
[36] J. Crank, The Mathematics of Diffusion, Oxford university press, 1979.
[37] D. Darmana, N.G. Deen, J. Kuipers, Detailed 3d modeling of mass transfer processes in two-phase flows with dynamic interfaces, Chem. Eng. Technol. 29 (2006) 1027–1033.
[38] G. Chen, C. Kharif, S. Zaleski, J. Li, Two-dimensional Navier–Stokes simulation of breaking waves 11(1) (1999) 121–133.